



Effect of grain size on the corrosion resistance of the Fe₄₁Mn₂₅Ni₂₄Co₈Cr₂ high entropy alloy

Ahmad Bahmani ^{a,*}, Shabnam Moradi ^a, Mehrab Lotfpour ^b, Hee Tae Jeong ^c, Woo Jin Kim ^{c,*}

^a Ultra-light Alloy Laboratory, Department of Advanced Materials and Renewable Energy, Iranian Research Organization for Science and Technology, Tehran 3313193685, Iran

^b Department of Mechanical Engineering, University of Nevada, Reno, NV 89557, USA

^c Department of Materials Science and Engineering, Hongik University, Mapo-gu, Sangsu-dong 72-1, Seoul 121-791, Republic of Korea



ARTICLE INFO

Keywords:

High entropy alloys
Corrosion properties
High-ratio differential speed rolling
Annealing

ABSTRACT

The annealing effect on the corrosion resistance of a non-equiautomic Fe₄₁Mn₂₅Ni₂₄Co₈Cr₂ high entropy alloy after high-ratio differential speed rolling was examined. The corrosion resistance of the alloy improved as the grain size decreased within the grain-size range of 3.5 μm to 84.9 μm. Grain boundaries were identified as contributing factors to the enhanced corrosion resistance by acting as barriers to corrosion pitting by inducing changes in crystallographic orientation. Additionally, grain boundaries facilitated the transportation of Cr ions to the surface by providing a pathway with a higher diffusivity and provided the nucleation sites of Cr oxide, leading to the formation of a more compact and evenly distributed corrosion layer on the surface of the alloy with a smaller grain size.

1. Introduction

High-entropy alloys (HEAs) have emerged as promising contenders to compete with conventional alloys [1]. Two primary distinctions set HEAs apart from traditional alloys [2,3]: (I) Composition: Traditional alloys typically consist of one primary element, with additional elements incorporated as per specific requirements. These compositions focus on optimizing properties in the vicinity of one side of the phase diagram, centered around the base elements. On the contrary, HEAs consist of five or more principal elements, arranged in equiautomic or non-equiautomic proportions, allowing for the exploration of extensive internal regions of the phase diagrams [4,5], and (II) Phases: In conventional alloys, the formation of complex intermetallic phases, which have a fixed stoichiometry and ordered atomic arrangement, is a common occurrence during the solidification and cooling process. In contrast, HEAs comprise disordered single- or multi-phase solid solutions, adopting face-centered cubic (FCC), body-centered cubic (BCC), or close-packed (HCP) structures. This is attributed to their high configurational entropy and low enthalpy of mixing [4–8].

It is well known that while the presence of secondary phase particles in the matrix of metals is often detrimental to corrosion resistance of metals, a uniform distribution of passivating elements, such as Cr, Ni, and Mo, within the solid solution matrix of metals enhances their

corrosion resistance [8,9]. In light of this, non-equiautomic and equiautomic FCC CoCrFeMnNi-based HEAs have attracted attention due to their possession of a single FCC solid solution phase enriched with corrosion-resistant elements and the absence (or limited presence) of secondary phase particles in the matrix. Several studies on the corrosion properties of HEAs are available [2,3,5,8]. Torbati-Sarraf et al. [4] studied the electrochemical behavior of two equiautomic HEAs, namely Cr_{22.8}Fe_{25.11}Co_{25.47}Ni_{26.4} and Cr_{19.37}Fe_{18.15}Co_{21.47}Ni_{21.32}Mn_{19.6} (wt%), at different temperatures in a 0.1 M NaCl solution. The results revealed that CrFeCoNi exhibited superior corrosion performance compared to CrFeCoNiMn alloy in the 0.1 M NaCl solution. The reduced corrosion resistance of the CrMnFeCoNi alloy was ascribed to the negative effect of Mn on corrosion and the lower concentration of beneficial passivating alloying element, Cr [4]. Yang et al. [5] conducted an investigation into the effect of Mn addition on the corrosion behavior of the CoFeNiMnCr HEA in a 0.1 M H₂SO₄ solution. Corrosion evaluations using potentiodynamic polarization and EIS revealed a significant degradation in the general corrosion resistance of the CoFeNiMnCr HEA upon the addition of Mn. This negative effect was mainly attributed to the influence of Mn on the passivation process, which considerably reduces the stability of the passive films. Wang et al. [9] studied the corrosion resistance of the equiautomic CoCrNi medium-entropy alloy (MEA) and conducted a comparative analysis with 304 stainless steel (SS) (composed of 71.41%

* Corresponding authors.

E-mail addresses: a.bahmani@irost.org (A. Bahmani), kimwj@wow.hongik.ac.kr (W.J. Kim).

Fe, 18.56% Ni, 8.93% Cr, and 0.89% Mn) in two H₂SO₄ and NaOH solutions. In the 1 M H₂SO₄ solution, the CoCrNi MEA exhibited significantly enhanced corrosion resistance compared to the 304 SS. This improvement was credited to the formation of a stable and thick Co-rich oxide layer on the surface of the CoCrNi MEA, serving as an effective corrosion barrier. However, in the 1.5 M NaOH solution, the corrosion resistance of the CoCrNi MEA decreased, performing poorer than the 304 SS. This degradation was primarily attributed to significant Cr element dissolution from the matrix of CoCrNi MEA into the solution [10]. Wu et al. [2] designed a non-equiautomic FCC Fe₄₀Ni₂₀Co₂₀Cr₂₀ (at %) HEA and compared its corrosion resistance with that of a 316 L SS (68.75%Fe, 18.47%Cr, 9.33%Ni, 2.03%Mn (at%)) in a 0.1 M H₂SO₄ solution. The non-equiautomic HEA exhibited higher corrosion resistance than the 316 L SS in electrochemical corrosion tests. This improved resistance was attributed to the higher fraction of Ni in the HEA, which promotes the formation of anti-corrosive Cr³⁺ species within the passive film.

The aforementioned results demonstrate the significant effect of altering the concentration of specific elements on the corrosion behavior of HEAs. In addition to compositional design, manipulating microstructures through thermomechanical working and heat treatments is also known to be crucial for improving the corrosion behavior of metals [9,11,12]. Among various microstructural parameters, grain size is widely acknowledged for playing an important role in the corrosion behavior of metals [13–15]. In the case of HEAs, as well as conventional metals, conflicting findings exist regarding the influence of grain size on their corrosion behavior. Positive effects of small grain size on the corrosion properties of HEAs have been reported by several investigators [10,11]. Jinlong et al. [10] examined the effect of solution heat treatment at different times and temperatures on the corrosion behavior of a cold-rolled CoCrNi MEA in a 0.1 M NaCl solution. Their findings revealed that grain refinement, achieved through heat treatment, led to a decrease in the passive current and an increase in the breakdown potential in the sodium chloride solution. Xue et al. [11] examined the corrosion behavior of a single-phase AlCrCuFe₅₃Ni₃₅ HEA subjected to cold rolling and subsequent annealing in a simulated seawater solution. Their results showed that reducing grain size enhanced the localized corrosion resistance of the material. Conversely, negative effects of small grain size on the corrosion properties of HEAs have also been reported [12–14]. Parakh et al. [12] found that grain boundaries provided potential sites for corrosion initiation, and thus increasing grain size improved corrosion resistance of the AlCoCrFeNi HEA. Han et al. [13] employed cryogenic rolling followed by short-time annealing to produce an ultra-fine-grained (UFG) equiautomic CoCrFeMnNi HEA. They found that the UFG HEA is more vulnerable to galvanic corrosion and pitting corrosion. Wang et al. [14] showed an increase in the corrosion resistance of the equiautomic CoCrFeMnNi HEA with increasing grain size. However, when the grain size was over $\geq 150 \mu\text{m}$, the corrosion resistance decreased due to the difficulty in forming a continuous and stable passive film on the surface.

Considering the inconsistency in the literature regarding the grain size effect on corrosion of HEAs, there is a compelling need for a comprehensive investigation into the effect of grain size on the corrosion properties of HEAs. While most corrosion studies have focused on equiautomic HEAs, non-equiautomic HEAs have received less attention. Furthermore, there are few reports on the corrosion studies of HEAs prepared by severe plastic deformation (SPD). SPD has proven to be an effective method for grain refinement and improving mechanical properties [15–18]. Recently, Jeong et al. [15] demonstrated that employing a rolling-based SPD (high-ratio differential speed rolling (HRDSR)) followed by annealing resulted in a superior combination of high strength and high uniform elongation in a non-equiautomic Fe₄₁Mn₂₅Ni₂₄Co₈Cr₂ HEA.

In the current study, samples with a wide range of grain sizes were prepared from non-equiautomic Fe₄₁Mn₂₅Ni₂₄Co₈Cr₂ HEA through the HRDSR process and subsequent annealing. The primary objective of this

research is to establish a relationship between grain size and corrosion properties of this alloy. By investigating this aspect, one can gain insights into the effect of severe plastic deformation and subsequent annealing on the corrosion behavior of HEAs, and understand the correlation between microstructural characteristics and corrosion resistance.

2. Materials and methods

An induction melting under vacuum produced a HEA ingot with a nominal composition of Fe₄₁Mn₂₅Ni₂₄Co₈Cr₂. After homogenization at 1100 °C for 13 h, the ingots were hot forged and then rolled from 10 mm to 3 mm in thickness with 8–10 passes using conventional rolling at 1000 °C. The rolled samples were heated to 1200 °C for 2 h to attain a fully recrystallized microstructure and subsequently quenched in water g. The heat-treated samples were then subjected to HRDSR (with a speed ratio of 2 between the upper roll and the lower roll) until reaching a final thickness of 0.7 mm. During the HRDSR process, the roll surfaces were preheated and kept at a temperature of 150 °C. After HRDSR, the samples underwent annealing at various temperatures for a duration of 1 h. The annealing temperatures ranged from 700 to 1200 °C, and the samples annealed at the corresponding temperatures were designated as A700, A800, A900, A1000, A1100, and A1200, where the numbers in the sample names represent the annealing temperature and 'A' represents annealed state.

Electron back-scattering diffraction (EBSD) analysis with scanning step sizes of 0.1–2.5 μm was used to characterize the microstructures after heat treatments (on the longitudinal sections of the samples parallel to the rolling direction). The EBSD data were processed using TSL-OIM analysis software, and the data points with a low confidence index (< 0.1) were eliminated from the EBSD data. For the grain size (*d*) evaluation, the tolerance angle was set to 15°.

The corrosion properties based on weight loss were obtained through a seven-day immersion test in a 3.5 wt% NaCl solution. The corrosion rate was calculated using the following relationship [22,23]:

$$CR = \frac{8.76 \times 10,000 \times \Delta W}{t \times A \times D} \quad (1)$$

where CR, ΔW, *t*, *A*, and *D* are the corrosion rate (mm/y), lost weight (mg), exposure time (day), exposed area (cm²) and density (g/cm³), respectively. Weight loss was measured by eliminating corrosion products through the use of an Aqua-regia solution, following the ASTM-G1 standard [23].

Electrochemical analysis was performed using an EG&G PARSTAT 2273 instrument after immersing the samples in a 3.5 wt% NaCl solution for 30 min. The analysis involved measurements of open circuit potential (OCP), potentiodynamic polarization, and electrochemical impedance spectrometry (EIS). EIS covered a frequency range from 100,000 Hz to 0.01 Hz, while potentiodynamic polarization tests were conducted in the potential range of ± 250 mV relative to the OCP with a scan rate of 1 mV/s.

XRD measurements were conducted on the samples before and after immersion using the FIRSTGUARD-RIGAKU instrument at 20° angles ranging from 20 to 80 degrees.

The surfaces of the samples were examined using a scanning electron microscope (SEM) before and after removing corrosion products to analyze change of surface morphology after corrosion.

All the samples utilized for weight loss tests, electrochemical tests, and EBSD and XRD analyses underwent the identical preparation process, which included sequential grinding with 400 to 2000-grit SiC paper, polishing with 0.1 μm diamond powder, and subsequent cleaning with deionized water and alcohol.

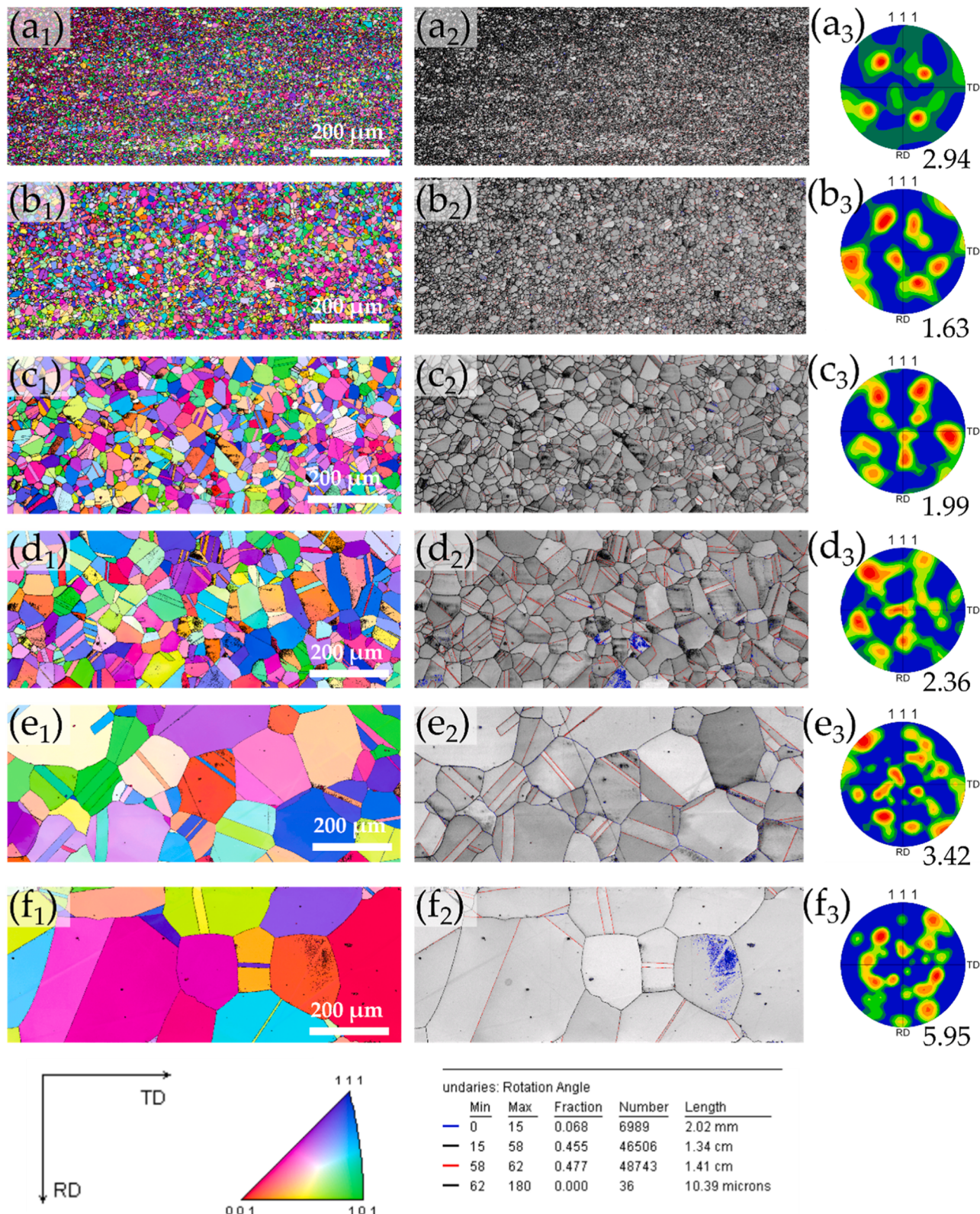


Fig. 1. EBSD inverse pole figure and grain boundary maps and (111) pole figures of the (a₁-a₃) A700, (b₁-b₃) A800, (c₁-c₃) A900, (d₁-d₃) A1000, (e₁-e₃) A1100, and (f₁-f₃) A1200 samples.

3. Results and discussion

3.1. Microstructures

Fig. 1 shows the inverse pole figure (IPF) and grain boundary (GB)

maps and (111) pole figures of the HRDSRed samples annealed in the temperature range between 700 and 1200 °C. After annealing at all temperatures, severely deformed microstructures underwent complete recrystallization, resulting in the formation of equiaxed grains with a random texture. Annealing twins, typically detected in FCC metals with

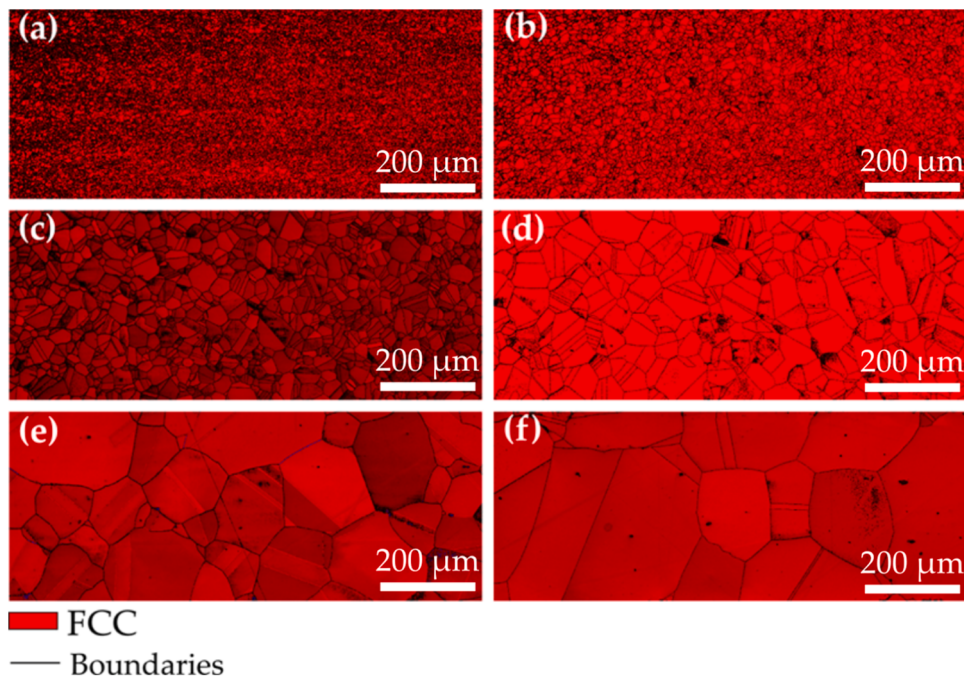


Fig. 2. EBSD phase maps of the (a) A700, (b) A800, (c) A900, (d) A1000, (e) A1100, and (f) A1200 samples.

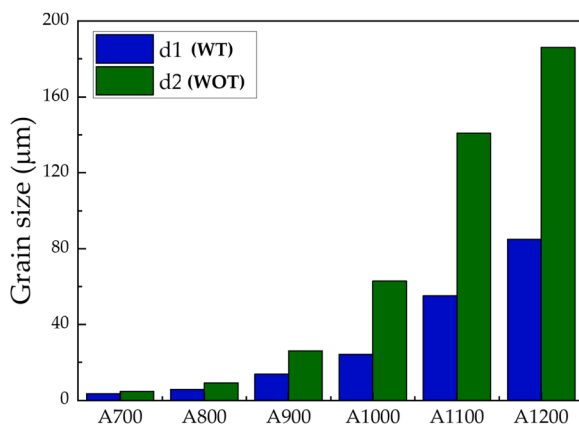


Fig. 3. Grain sizes of the annealed HEA. d1 and d2 are the grain sizes determined with (WT) and without (WOT) considering twin boundaries, respectively.

low or medium stacking fault energies (SFEs) [21], are observed to have formed in the recrystallized grains. **Fig. 2** shows the phase maps of the annealed samples, revealing the exclusive presence of a single FCC phase regardless of the annealing temperature.

Fig. 3 shows the average grain sizes of the annealed samples. The measurements were carried out with (WT) and without (WOT) considering the twin boundaries. It is apparent that the grain size increases with rise in annealing temperature, regardless of whether twin boundaries are taken into account or not. The smallest grain size of 3.5 (4.6) μm is obtained from A700, while the largest grain size obtained of 84.9 (186.1) μm is obtained from A1200.

The Kernel Average Misorientation (KAM) value represents local misorientation inside grains attributed to the presence of geometrically necessary dislocations [19] (**Fig. 4**). The blue area in the KAM maps illustrates the region with low dislocation density, supporting that the alloys became fully recrystallized after annealing at all the temperatures. There are, however, black regions near some grain boundaries in the KAM maps, where CI values are less than 0.1. These areas may

represent the presence of non-equilibrium grain boundaries or other defects that disrupt the normal diffraction patterns. The unindexed area in the KAM maps tends to decrease as the annealing temperature increases.

3.2. Corrosion behaviors

3.2.1. Weight loss tests

Fig. 5 and **Table 1** present the corrosion rates (based on weight loss) of the samples after immersion in a 3.5 wt% NaCl solution for seven days. The results show that the corrosion rate tends to increase with increasing annealing temperatures, which can be interpreted as an indication that the corrosion rate increases with an increase in grain size. This observation is often noted in conventional metals [19–21], suggesting that grain size significantly affects the corrosion rate, and reducing the grain size enhances corrosion resistance.

Fig. 6 shows the low and high magnification SEM micrographs of the alloys immersed for even days in a 3.5 wt% NaCl solution. Overall, the A800 and A900 samples exhibit the least corrosion. All samples display a distinct band-like region (BLR) between corroded and uncorroded areas, indicated by white arrows, representing the corrosion frontier on the surface exposed to the solution. Additionally, signs of pitting corrosion and granular corrosion are observed.

3.2.2. EIS tests

Fig. 7 shows the open circuit potential (OCP) curves of the samples annealed at different temperatures. Some samples exhibit potential fluctuations during the early stages of immersion, but they stabilize afterward. Among the samples, the A900 sample exhibits the highest OCP after stabilization, suggesting the formation of the most stable corrosion layer on the surface, while the A1200 sample reveals the lowest OCP.

The electrochemical impedance spectroscopy (EIS) results for the annealed HEAs are presented in **Fig. 8**. Among the Bode plots shown in **Fig. 8(a)**, the A700 sample exhibits a contrasting behavior compared to the other samples. It displays high resistance at medium frequencies but experiences a sudden drop in resistance at low frequencies. **Fig. 8(b)** presents the Nyquist plots for the samples annealed at different temperatures. In the case of the A800, A900, A1000, A1100, and A1200 samples, a depressed capacitance arc (not a perfect semicircle) is

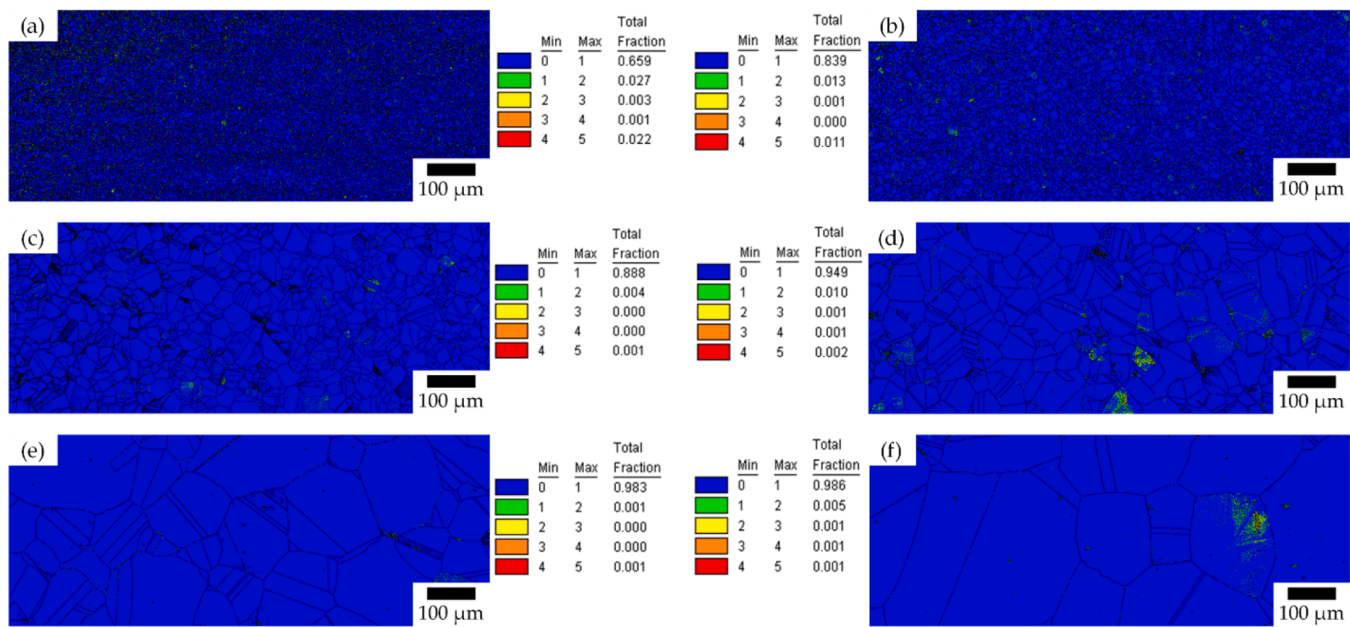


Fig. 4. Kernel Average Misorientation (KAM) maps of the (a) A700, (b) A800, (c) A900, (d) A1000, (e) A1100, and (f) A1200 samples.

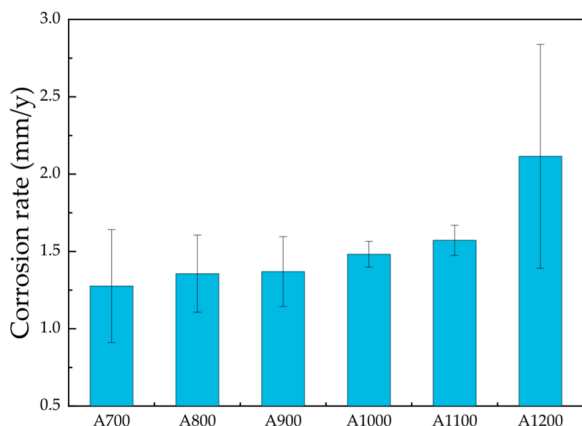


Fig. 5. Corrosion rates of different samples calculated based on the weight loss after immersion in a 3.5 wt% NaCl solution for seven days.

Table 1

The corrosion rate values (mm/y) for the annealed samples calculated based on the weight loss measurements.

Samples	Set 1	Set 2	Set 3	Average
A700	1.07	1.05	1.69	1.27 ± 0.36
A800	1.17	1.26	1.64	1.35 ± 0.24
A900	1.29	1.20	1.62	1.37 ± 0.22
A1000	1.43	1.58	1.43	1.48 ± 0.08
A1100	1.49	1.54	1.68	1.57 ± 0.09
A1200	1.90	1.52	2.92	2.11 ± 0.72

observed in the high-frequency range, followed by an incomplete capacitance arc in the low-frequency range. The diameter of the capacitance arc decreases in the following order: A800, A900, A1200, A1100, and A1000, implying that the A800 and A900 samples exhibit better corrosion resistance compared to the other samples in comparison. In contrast, the A700 sample shows a depressed capacitive loop in the high-frequency range and an inductive loop in the low-frequency range.

The Nyquist plots derived from the EIS measurements were fit using

EC-Lab V10.40 commercial software, and the corresponding fitted plots are shown as solid lines in Fig. 8(b). Two types of equivalent circuit models were generated from the fitted EIS data, as shown in Fig. 8(c): c_1 is for the A700 sample and c_2 is for the other samples. In the equivalent circuits, R_s represents the resistance of the solution, R_{cp} represents the resistance of the corrosion product layer and R_{ct} represents the charge transfer resistance. CPE1 corresponds to a constant phase element that runs in parallel with R_{cp} , while CPE2 is associated with another constant phase element running in parallel with R_{ct} . CPEs are typically attributed to mass transport processes occurring in the solid phase, indicating the presence of diffusion resistance. These elements contribute to deviations from ideal dielectric properties, which may arise from surface inhomogeneity or current leakage on the surface [24–26]. An inductive element (L), running parallel to R_L , in c_1 is related to the formation, adsorption, and desorption of corrosion products on the surface of the sample, which is mainly observed at lower frequencies. The presence of this inductive element indicates that corrosion occurs on the surface, specifically at cracks and discrete sites, involving a complex intermediate process rather than a basic charge transfer mechanism.

The resulting parameters obtained from the fitted equivalent circuits in Fig. 8(c₁) and Fig. 8(c₂) are listed in Table 2. Both the A800 and A900 samples exhibit the largest R_{cp} values among all the samples annealed at temperatures above 800°C, indicating the highest protection ability of their surface layers.

Using the Brug's equation (Eq. (2)) [6,22,23], the effective capacitance of the double layer (C_{dl}) can be calculated:

$$C_{dl} = CPE_2^{1/\alpha_2} \left(\frac{1}{R_s} + \frac{1}{R_{ct}} \right)^{\frac{\alpha_2-1}{\alpha_2}} \quad (2)$$

The effective capacitance of the passive layer (C_{cp}), on the other hand, can be calculated using the Hsu-Mansfeld equation (Eq. 3) [6,24, 25]:

$$C_{cp} = CPE_1 (\omega')^{\alpha_1-1} \quad (3)$$

where ω' is the angular frequency at which the imaginary part of impedance is maximum. Once C_{cp} is calculated, the passive film thickness (d_p) can be determined using Eq. (4) [26]:

$$d_p = \frac{\epsilon \epsilon_0}{C_{cp}} \quad (4)$$

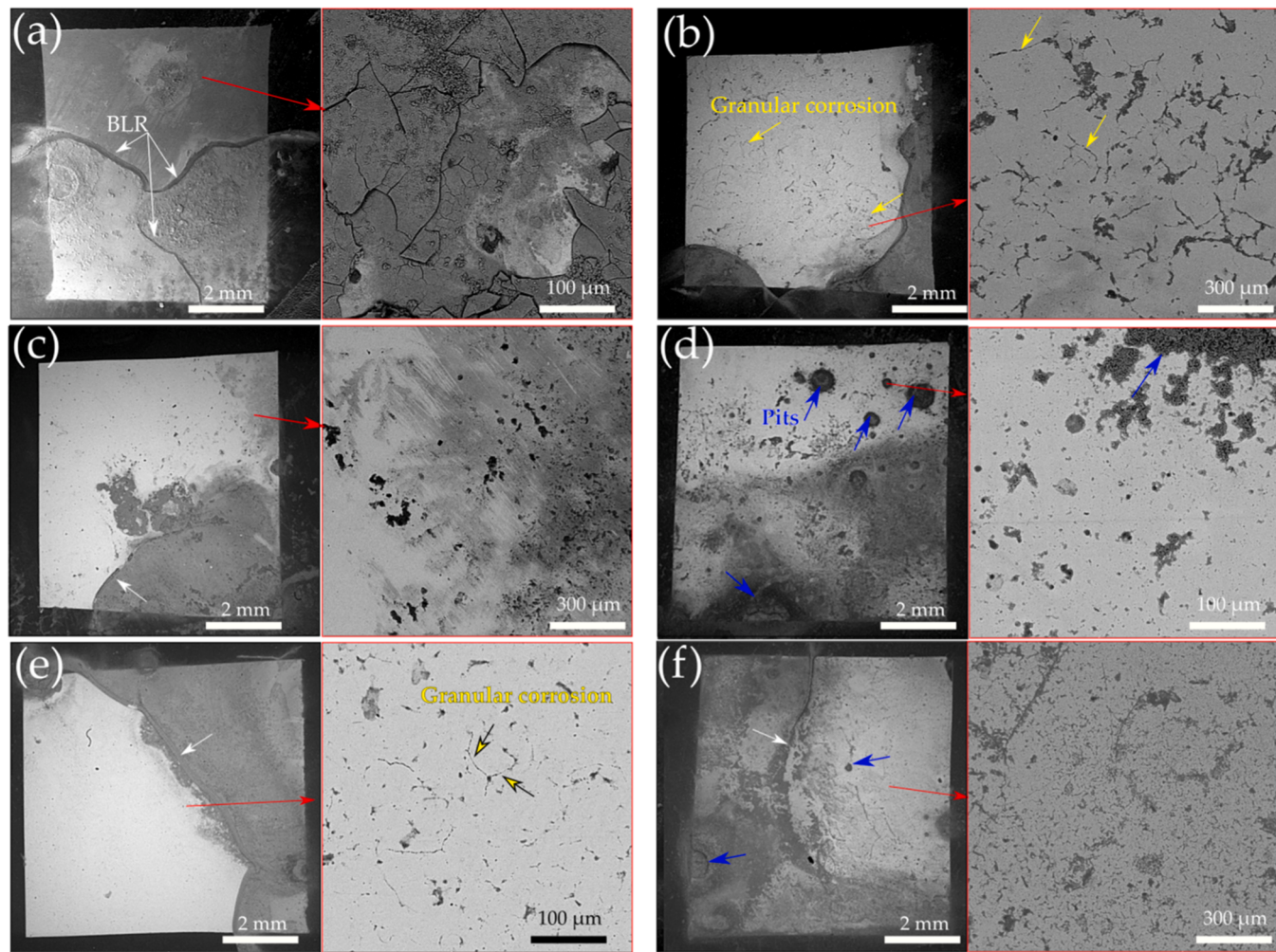


Fig. 6. Low and high magnification SEM micrographs of the (a) A700, (b) A800, (c) A900, (d) A1000, (e) A1100, and (f) A1200 samples, immersed in 3.5 wt% NaCl solution for seven days.

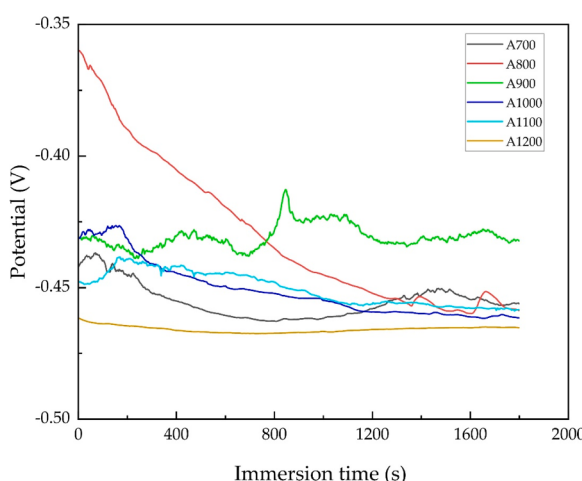


Fig. 7. Open circuit potential (OCP) curves of the samples annealed at different temperatures.

where ϵ and ϵ_0 represent the relative permittivity of the passive film and the vacuum permittivity, respectively, which are set to 30 and 8.85×10^{-14} (F/cm), respectively [26]. The calculated values of C_{dl} , C_{cp} and d_p are presented in Table 2. The analysis results show that the

A800 and A900 samples have the thickest passive layer, whereas the A1200 sample has the thinnest.

3.2.3. Potentiodynamic polarization tests

Fig. 9 represents the polarization curves of the samples annealed at different temperatures. The cathodic branches of all the samples lack linear segments, posing a challenge in measuring corrosion current. Many HEAs exhibit complex cathodic branch curves [26,27]. This complexity often arises from various factors, including competition among multiple cathodic reactions and mass transport limitations [28]. The corrosion potential (E_{corr}) increases with increasing annealing temperature from 700 to 900 °C, but then experiences a sudden decrease and remains nearly constant at higher annealing temperatures (1000–1200 °C). The increase in E_{corr} with increasing annealing temperature from 700 to 900 °C suggests an improved formation of a passive layer, whereas the decrease in E_{corr} at annealing temperatures above 1000 °C indicates a reduction in the surface layer resistance. Passivation-pitting, characterized by a sharp rise in current density at high potentials in the polarization curves, occurred in all samples except for A800 and A900, indicating that these two samples were less affected by passivation-pitting. Unlike the A800 and A900 samples, however, the sample A700 exhibits passivation-pitting despite its small grain size. This could be attributed to the presence of non-equilibrium grain boundaries and high-density dislocations near grain boundaries that remained after annealing at 700 °C (Fig. 4a). High residual stress may develop in defect areas, leading to the initiation and propagation of

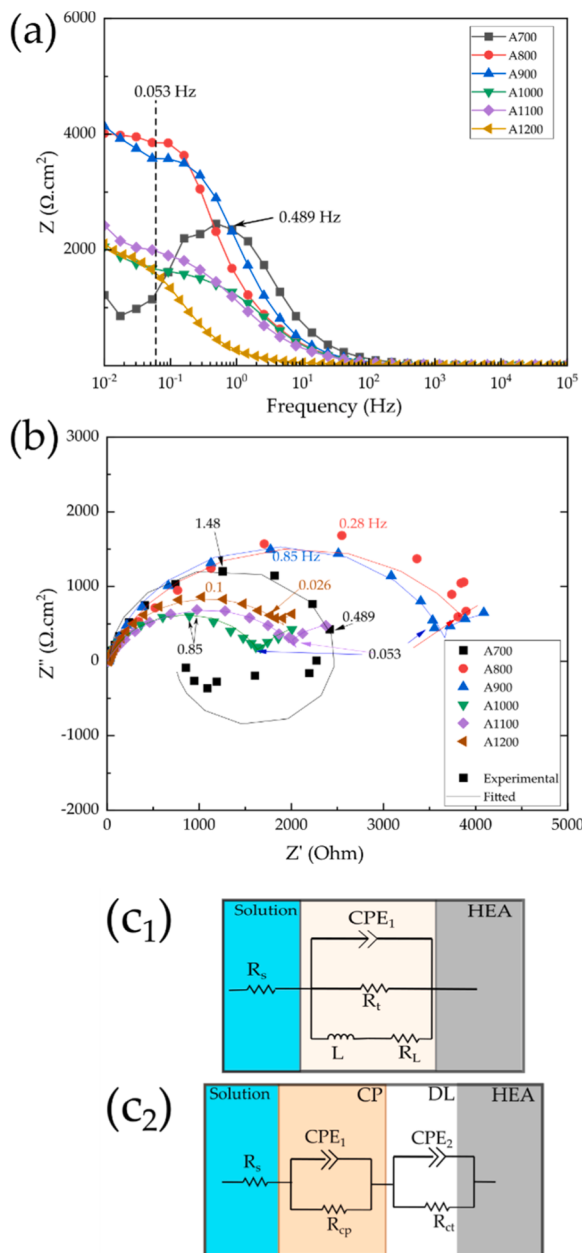


Fig. 8. Results of the EIS tests: (a) Bode, (b) Nyquist plots, (c₁) Equivalent circuit model from the fitted EIS data for A700 and (c₂) Equivalent circuit model from the fitted EIS data for the other samples.

cracks in the passive oxide layer [32,33], deteriorating its protective properties.

Furthermore, the cathodic branch of the polarization curve of A700 exhibits a significant leftward shift compared to those of the other samples. This highly reduced cathodic current in A700 may be linked to

Table 2

Values of the parameters measured from the Nyquist curves of the annealed samples.

Samples	R _s (Ω·cm ²)	CPE1 (μF.s (α ⁻¹))	α ₁	R _{cp} (Ω·cm ²)	CPE2 (μF.s (α ⁻¹))	α ₂	R _{ct} (Ω·cm ²)	L (H)	R _L (Ω·cm ²)	C _{dl} (μF·cm ⁻²)	C _{cp} (μF·cm ⁻²)	d _p (nm)
A700	27.06				30.3		0.866	2557	4887	987.1	10.1	-
A800	13.84	114.0	0.788	4256	2836	0.656	4682			3.85	101.1	6.91
A900	16.34	64.3	0.846	3759	5329	0.721	2219			4.51	49.7	5.89
A1000	9.07	98.8	0.804	1706	9810	0.737	1509			8.06	63.8	3.30
A1100	1.94	158.5	0.722	2159	11920	0.864	1216			44.5	99.4	0.60
A1200	9.51	746.1	0.830	2181	9489	0.834	1900			278.4	807.4	0.09

the instability of the passive layer, which limits the effectiveness of cathodic processes over the surface. It is worth noting that the high E_{corr} and absence of passivation-pitting in the A800 and A900 samples, as indicated by their polarization curves, align with their large R_{cp} and d_p values obtained from the EIS analyses.

3.3. Observation of the surface of the samples after the immersion tests

Fig. 10 (a) shows the XRD curves of the samples after immersion in a 3.5 wt% NaCl solution and **Fig. 10 (b)** shows the XRD curve of the A700 sample before the immersion. As observed, XRD curves exhibit several new peaks after immersion, corresponding to Mn, Cr, and Fe oxides.

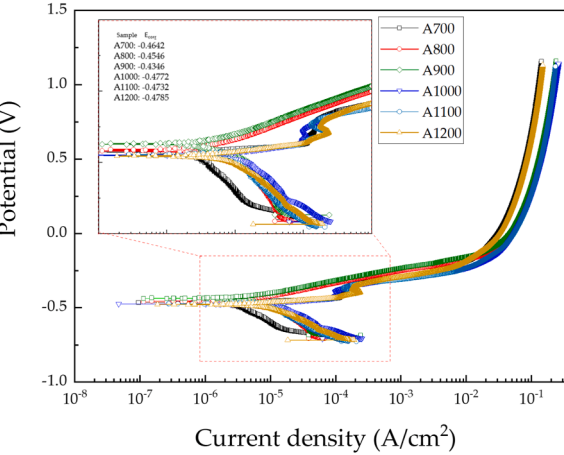


Fig. 9. Polarization curves of the samples annealed at different temperatures.

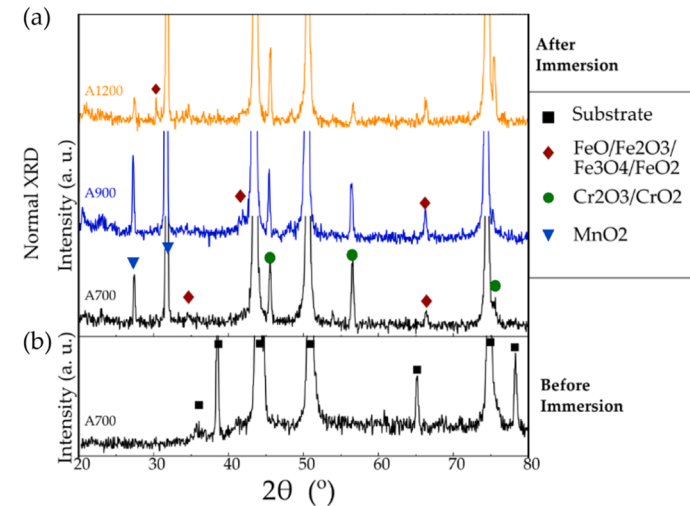


Fig. 10. XRD curves for (a) the A700, A900 and A1200 samples after the 7 day immersion and (b) the A700 sample before the immersion.

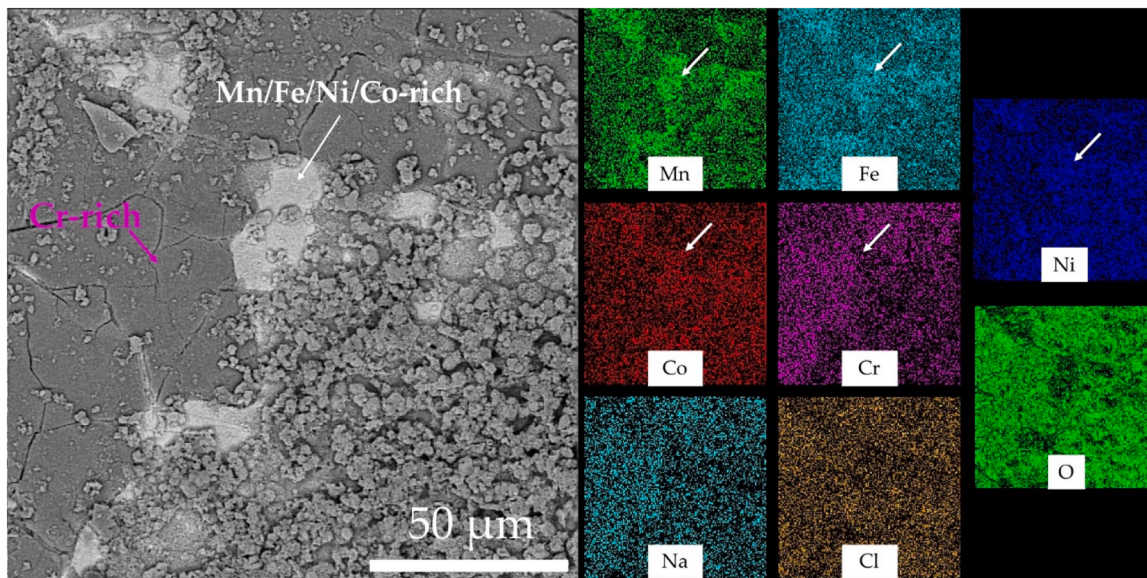


Fig. 11. SEM and EDS mapping analysis of the A700 sample after 7 days of immersion.

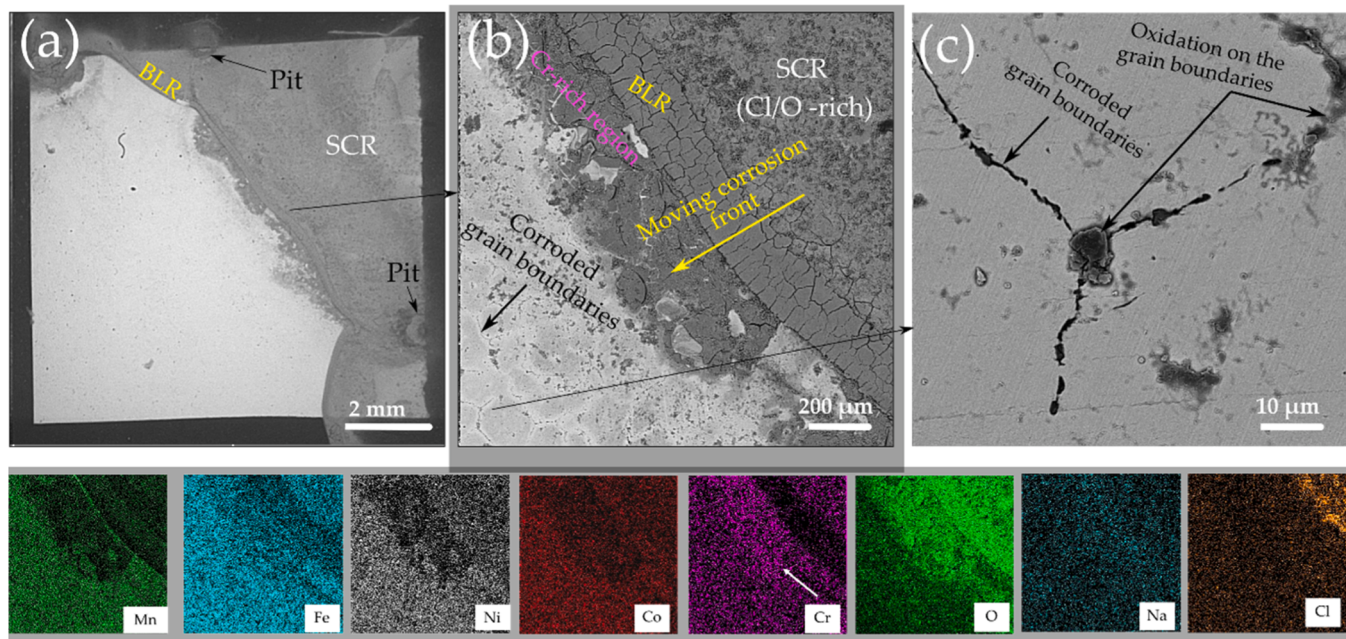


Fig. 12. SEM and EDS mapping analysis of the A1100 sample after 7 days of immersion.

Fig. 11 shows the SEM and EDS mapping analysis for the corroded surface of A700 after the 7 days of immersion. The SEM image displays various regions with distinct levels of corrosion. The brighter regions, indicated by a white arrow, consist of a mixture of Mn, Fe, Ni, and Co oxides (predominantly Mn and Fe oxides according to the XRD curves in **Fig. 10**). On the left side of the SEM image, the desert-like area shows an enrichment of chromium and oxygen, indicating the presence of chromium oxides. These observations suggest that Cr, Mn, and Fe undergo reactions with oxygen, leading to the formation of oxides on the surface. Cr_2O_3 is well recognized for its ability to form a protective layer on the surface of materials during corrosion, acting as a barrier that provides corrosion resistance and prevents further deterioration of the underlying material. Cracks are commonly observed in the desert-like regions, indicating the susceptibility of Cr_2O_3 layer to cracking. Cracks are also evident in the optical micrograph of A700 after immersion, as shown in

Fig. 6(a). This observation suggests that the inductive loop observed in the EIS curve for A700 is likely associated with cracking of Cr_2O_3 during corrosion. In addition to the aforementioned two regions, there is a region covered with nodule-like corrosion products (shown on the right side of the SEM image), primarily composed of iron oxides.

Fig. 12 shows the SEM and EDS mapping analysis for the corroded surface of A1100 after 7 days of immersion. It reveals the presence of three distinct regions. The first region corresponds to the severely corroded region (SCR), which is distinguished by an enrichment of Cl and O elements and has experienced more extensive corrosion compared to the other regions. The second region, identified as the Cr and O-rich region (CRR), signifies the presence of Cr oxide layer. **Fig. 12(c)** represents a magnified view of a small area on the left side of the image in **Fig. 12(b)**. Corrosion products can be observed on the grain boundaries, appearing darker in color (among the present alloying elements, Cr is

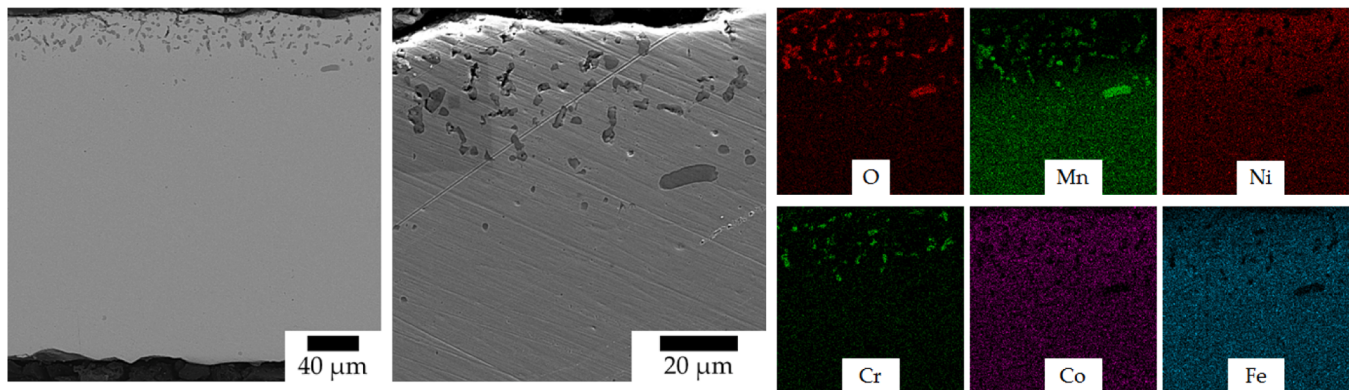


Fig. 13. The cross-sectional SEM and EDS analysis of the A1100 sample after 7 days of immersion.

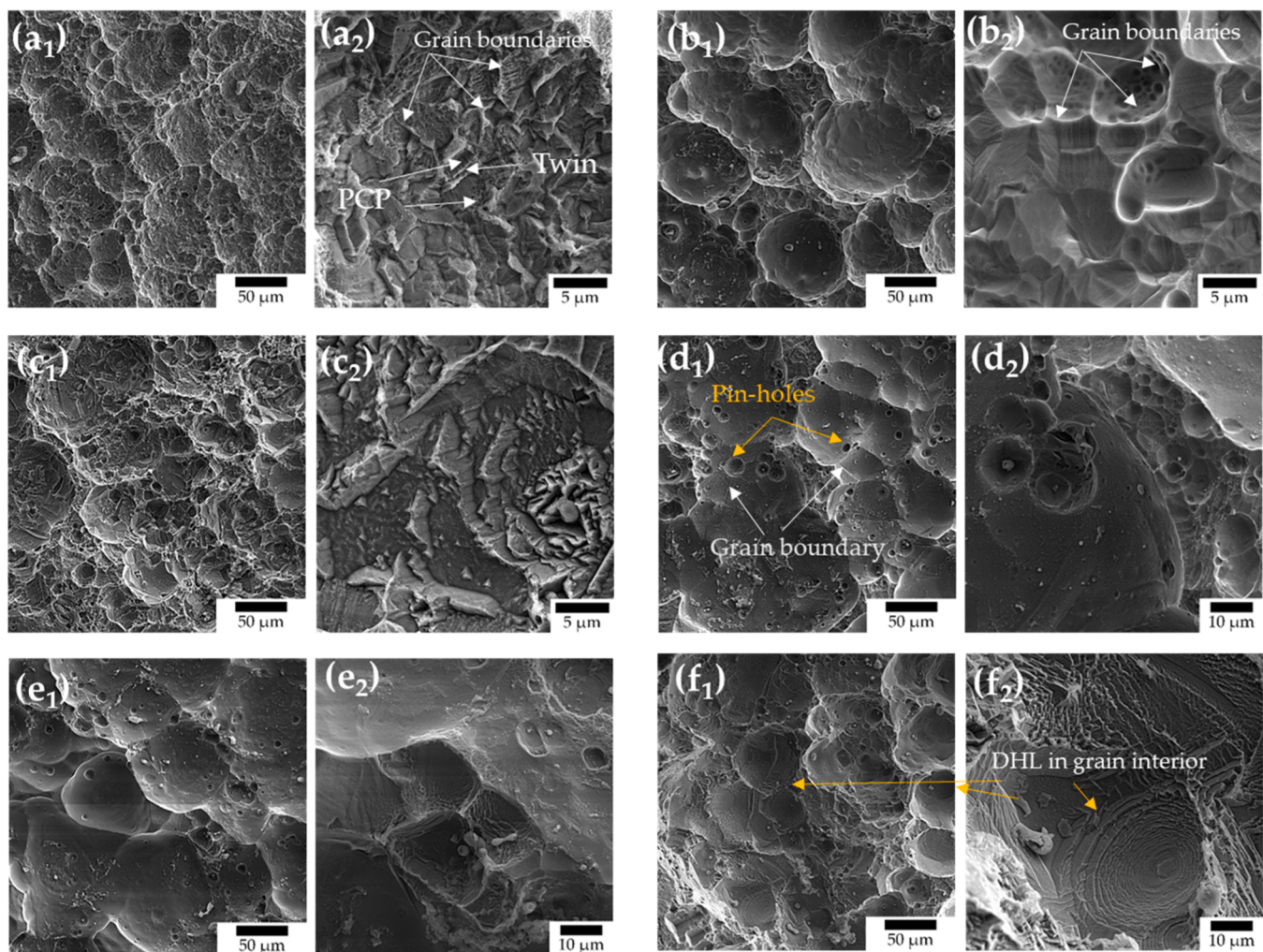


Fig. 14. Low and high magnifications SEM micrographs of (a) A700, (b) A800, (c) A900, (d) A1000, (e) A1100, and (f) A1200 samples after removing the corrosion products.

the lightest, leading to a darker appearance in backscattered images when enriched), which suggests formation of Cr oxide. This observation indicates that chromium oxide preferentially forms along grain boundaries rather than uniformly covering the surface, in contrast to A700 where a significant portion of the surface is uniformly covered with chromium oxide. The third region is a band-like region (BLR) located between the SCR and the CRR. The BLR can also be observed in other samples (marked by white arrows in Fig. 6). While the SCR can be

distinguished by its Cl-rich composition, indicating that Cl ions have attacked the oxide layer, no signs of Cl ions can be found within the BLR. The BLR shows a higher concentration of oxygen but is depleted in chromium. The chromium atoms may have migrated to adjacent regions, leading to the formation of the Cr-rich CRR that impedes the propagation of corrosion.

Fig. 13 presents the cross-sectional SEM and EDS analysis for the corroded surface of A1100 after 7 days of immersion. The formation of a

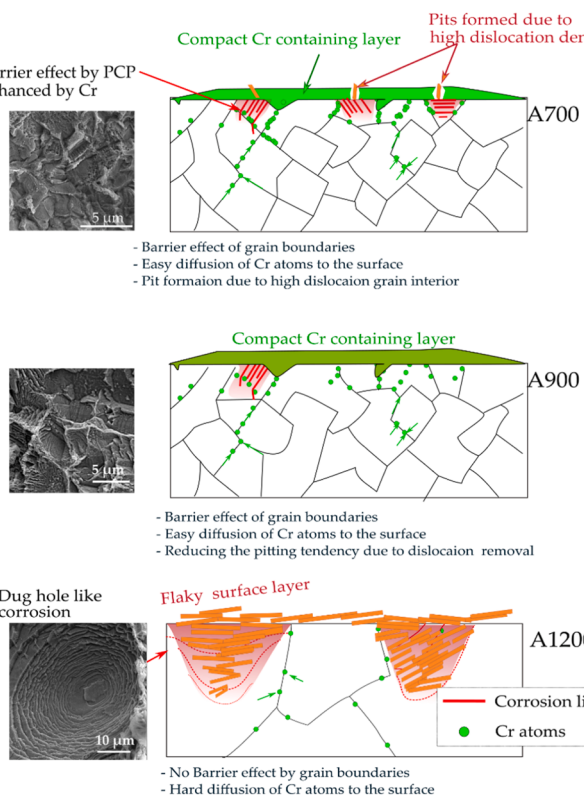


Fig. 15. Schematic drawing for the corrosion mechanisms observed in the current HEAs with different grain sizes.

continuous oxide layer on the surface of the sample is not obvious. Instead, the formation of chromium oxide and manganese oxide in the form of particles is evident. Cr and Mn have a stronger tendency to form oxides compared to Ni and Co, attributed to their higher standard reduction potentials and greater affinity for undergoing reduction reactions, especially in the presence of oxygen. Studies have demonstrated that both Mn and Cr can enhance the corrosion resistance of iron [34–36]. However, since the chromium oxide and manganese oxide exist in the form of particles, their contribution to acting as a barrier against corrosion is expected to be low, which agrees with the results of the immersion and electrochemical tests.

Fig. 14 presents low and high magnification SEM micrographs of the annealed samples after the removal of corrosion products. The low magnification micrographs reveal the presence of holes on the surfaces, and their size increases with increasing annealing temperatures (i.e., increasing grain size). The high-magnification SEM micrographs exhibit the grain boundary corrosion features in the A700, A800, and A900 samples. The A700 sample displays parallel lines within the grain interior, which can be attributed to the occurrence of preferred crystallographic pitting (PCP) [20,21]. However, as the annealing temperature increases (i.e., with an increase in grain size), the PCP becomes less pronounced, and dug-hole-like (DHL) features appear, indicating degradation of the grain interior. These observations suggest that the A700, A800, and A900 samples primarily undergo grain boundary corrosion due to their high-density grain boundaries, while the A1000, A1100, and A1200 samples with coarse grains experience degradation primarily within the grain interiors.

Fig. 15 schematically illustrates the corrosion mechanism observed in the annealed samples with small and large grain sizes. Grain boundaries can play a crucial role in altering the corrosion resistance of the alloy. First, they act as barriers to the corrosion pitting by causing changes in crystallographic orientation through PCP mechanism [1,2]. This orientation change hinders the progression of corrosion pits. Second, grain boundaries facilitate the transport of the Cr element by

providing a pathway with higher diffusivity. The chromium element is recognized for its high capability to form a protective passive layer through its reaction with oxygen. Samples with small grain sizes have a higher density of grain boundaries. Consequently, Cr^{n+} ions are more efficiently released into the exposed surface through grain boundaries. Therefore, the passive film can nucleate at numerous nucleation sites, leading to the uniform formation of a dense and compact passive Cr oxide layer across the entire surface. This results in a rapid thickening of the passive film. In contrast, samples with larger grains are more susceptible to pitting corrosion. This vulnerability can be attributed to the reduced concentration of Cr^{n+} ions in the corrosion medium on the surface of the sample with low density of grain boundaries and a decrease in the number of nucleation sites for Cr oxide, thereby resulting in the uneven growth and thin thickness of Cr oxide layer. The A700 sample, despite having the smallest grain size, does not exhibit a clear advantage compared to the A800 and A900 samples in corrosion resistance. This is because of the presence of high-density dislocations near grain boundaries and non-equilibrium grain boundaries that remained after annealing at 700 °C, causing the formation of pits and cracks on the Cr oxide layer.

4. Conclusions

The effects of annealing temperatures on the corrosion properties of the $\text{Fe}_{41}\text{Mn}_{25}\text{Ni}_{24}\text{Co}_8\text{Cr}_2$ high entropy alloy were investigated, leading to the following conclusions:

1. The EBSD analysis showed that the grain size increased with increasing annealing temperatures. The A700 sample has the smallest grain size of 3.5 μm and the A1200 sample has the largest grain size of 84.9 μm. All the annealed samples have the nearly fully recrystallized microstructures. However, in local regions near grain boundaries, high-density defects persisted to remain after annealing at 700 °C. The density of these defects decreased with increasing annealing temperatures.
2. The corrosion rates, obtained through immersion tests, EIS, and polarization tests, showed a decrease with decreasing grain size. The EIS data revealed the formation of the superior protective layer on the surfaces of the A800 and A900 samples, attributed to their small grain sizes and the effective removal of defects during annealing. This result aligns with that of the potentiodynamic study, where no passivation-pitting was observed in the A800 and A900 samples, while passivation-pitting was observed in the other samples.
3. Grain boundaries were observed to contribute to corrosion resistance by acting as barriers to corrosion pitting through changes in crystallographic orientation. They also facilitated the transportation of Cr elements to the surface by providing a pathway with a higher atomic diffusivity, leading to high concentration of Cr ions on the surface. Smaller grains also provide numerous nucleation sites for Cr oxide. These factors enable the formation of a compact and evenly distributed corrosion layer on the surface of the samples, resulting in a decreased corrosion rate.
4. When the grain size became large, the corrosion mechanism changed from grain boundary corrosion to corrosion within the grain interior.

Funding

This research was financially supported by the Mid-Career Researcher Program through the National Research Foundation of Korea funded by the Ministry of Education, Science and Technology (NRF-2020R1A2C1008105) and Ultra-light Alloys Laboratory (ULAL), Iranian Research Organization for Science and Technology (IROST).

CRediT authorship contribution statement

Jeong H. T.: Resources, Investigation. Kim W.J.: Writing – review &

editing, Resources, Conceptualization. **Moradi Shabnam:** Investigation. **Lotfpour Mehrab:** Investigation. **Bahmani Ahmad:** Writing – original draft, Methodology, Investigation, Formal analysis.

Declaration of Competing Interest

The authors declare that they have no known competing financial interests or personal relationships that could have appeared to influence the work reported in this paper.

Data Availability

Data will be made available on request.

References

- [1] K. Biswas, J.-W. Yeh, P.P. Bhattacharjee, J.T.M. DeHosson, High entropy alloys: Key issues under passionate debate, *Scr. Mater.* 188 (2020) 54–58.
- [2] P. Wu, K. Gan, D. Yan, Z. Fu, Z. Li, A non-equiautomic FeNiCoCr high-entropy alloy with excellent anti-corrosion performance and strength-ductility synergy, *Corros. Sci.* 183 (2021) 109341.
- [3] H. Luo, Z. Li, A.M. Mingers, D. Raabe, Corrosion behavior of an equiautomic CoCrFeMnNi high-entropy alloy compared with 304 stainless steel in sulfuric acid solution, *Corros. Sci.* 134 (2018) 131–139.
- [4] H. Torbati-Sarraf, M. Shabani, P.D. Jablonski, G.J. Pataky, A. Poursaei, The influence of incorporation of Mn on the pitting corrosion performance of CrFeCoNi High Entropy Alloy at different temperatures, *Mater. Des.* 184 (2019) 108170.
- [5] J. Yang, J. Wu, C.Y. Zhang, S.D. Zhang, B.J. Yang, W. Emori, J.Q. Wang, Effects of Mn on the electrochemical corrosion and passivation behavior of CoFeNiMnCr high-entropy alloy system in H₂SO₄ solution, *J. Alloy. Compd.* 819 (2020) 152943.
- [6] P. Gong, D. Wang, C. Zhang, Y. Wang, Z. Jamili-Shirvan, K. Yao, X. Wang, Corrosion behavior of TiZrHfBeCu(Ni) high-entropy bulk metallic glasses in 3.5 wt % NaCl, *npj Mater. Degrad.* 6 (1) (2022).
- [7] Y. Shi, L. Collins, R. Feng, C. Zhang, N. Balke, P.K. Liaw, B. Yang, Homogenization of Al_xCoCrFeNi high-entropy alloys with improved corrosion resistance, *Corros. Sci.* 133 (2018) 120–131.
- [8] Y. Zhang, T.T. Zuo, Z. Tang, M.C. Gao, K.A. Dahmen, P.K. Liaw, Z.P. Lu, Microstructures and properties of high-entropy alloys, *Prog. Mater. Sci.* 61 (2014) 1–93.
- [9] J. Wang, W. Li, H. Yang, H. Huang, S. Ji, J. Ruan, Z. Liu, Corrosion behavior of CoCrNi medium-entropy alloy compared with 304 stainless steel in H₂SO₄ and NaOH solutions, *Corros. Sci.* 177 (2020) 108973.
- [10] L. Jinlong, T. Zhiheng, T. Liu, The effect of the grain refinement on the corrosion resistance of the CoCrNi medium-entropy alloy in chloride solution, *Intermetallics* 141 (2022) 107423.
- [11] L. Xue, Y. Ding, K.G. Pradeep, R. Case, H. Castaneda, M. Paredes, The grain size effect on corrosion property of Al2Cr5Cu5Fe5Ni35 high-entropy alloy in marine environment, *Corros. Sci.* 208 (2022) 110625.
- [12] A. Parakh, M. Vaidya, N. Kumar, R. Chetty, B.S. Murty, Effect of crystal structure and grain size on corrosion properties of AlCoCrFeNi high entropy alloy, *J. Alloy. Compd.* 863 (2021) 158056.
- [13] Z. Han, W. Ren, J. Yang, A. Tian, Y. Du, G. Liu, R. Wei, G. Zhang, Y. Chen, The corrosion behavior of ultra-fine grained CoNiFeCrMn high-entropy alloys, *J. Alloy. Compd.* 816 (2020) 152583.
- [14] Y. Wang, J. Jin, M. Zhang, X. Wang, P. Gong, J. Zhang, J. Liu, Effect of the grain size on the corrosion behavior of CoCrFeMnNi HEAs in a 0.5 M H₂SO₄ solution, *J. Alloy. Compd.* 858 (2021).
- [15] H.T. Jeong, W.J. Kim, Microstructures and mechanical properties of the non-equiautomic FeMnNiCoCr high entropy alloy processed by differential speed rolling, *Mater. Sci. Eng.: A* 727 (2018) 38–42.
- [16] H. Shahmir, T. Mousavi, J. He, Z. Lu, M. Kawasaki, T.G. Langdon, Microstructure and properties of a CoCrFeNiMn high-entropy alloy processed by equal-channel angular pressing, *Mater. Sci. Eng.: A* 705 (2017) 411–419.
- [17] A. Bahmani, S. Arthanari, K.S. Shin, Improvement of corrosion resistance and mechanical properties of a magnesium alloy using screw rolling, *J. Alloy. Compd.* 813 (2020) 152155.
- [18] A. Bahmani, W.-J. Kim, Effect of Grain Refinement and Dispersion of Particles and Reinforcements on Mechanical Properties of Metals and Metal Matrix Composites through High-Ratio Differential Speed Rolling, *Materials* 13 (18) (2020).
- [19] A. Bahmani, S. Arthanari, K.S. Shin, Formulation of Corrosion Rate of Magnesium Alloys Using Microstructural Parameters, *J. Magnes. Alloy.* (2020).
- [20] A. Bahmani, M. Lotfpour, M. Taghizadeh, W.-J. Kim, Corrosion behavior of severely plastically deformed Mg and Mg alloys, *J. Magnes. Alloy.* (2022).
- [21] G. Han, J.-Y. Lee, Y.-C. Kim, J.H. Park, D.-I. Kim, H.-S. Han, S.-J. Yang, H.-K. Seok, Preferred crystallographic pitting corrosion of pure magnesium in Hanks' solution, *Corros. Sci.* 63 (2012) 316–322.
- [22] G.J. Brug, A.L.G. van den Eeden, M. Sluyters-Rehbach, J.H. Sluyters, The analysis of electrode impedances complicated by the presence of a constant phase element, *J. Electroanal. Chem. Interfacial Electrochem.* 176 (1) (1984) 275–295.
- [23] B. Tribollet, Analysis of Constant Phase Element, 223rd ECS Meeting, The Electrochemical Society, 2013.
- [24] C.H. Hsu, F. Mansfeld, Technical note: concerning the conversion of the constant phase element parameter Y₀ into a capacitance, *Corrosion* 57 (9) (2001) 747–748.
- [25] M.E. Orazem, N. Pébère, B. Tribollet, Enhanced graphical representation of electrochemical impedance data, *J. Electrochem. Soc.* 153 (4) (2006) B129.
- [26] Y. Fu, C. Dai, H. Luo, D. Li, C. Du, X. Li, The corrosion behavior and film properties of Al-containing high-entropy alloys in acidic solutions, *Appl. Surf. Sci.* 560 (2021).
- [27] Yao Qiu, M.A.G. Sebastian Thomas, Hamish L. Fraser, N. Birbilis, Corrosion of high entropy alloys, *Mater. Degrad.* (2017) 15.
- [28] Ca Ma, Y. Jin, M. Shi, Y. Chu, Y. Xu, W. Jia, Q. Yuan, J. Chen, D. Chen, S. Chen, Study of nano-WO₃modified carbon nanotubes supported Pt electrocatalyst for oxygen reduction reaction, *J. Electrochem. Soc.* 161 (3) (2013) F246–F251.